



Cite this: *Lab Chip*, 2019, 19, 1860

Tumor antigen-independent and cell size variation-inclusive enrichment of viable circulating tumor cells†

Wujun Zhao,[‡] Yang Liu,[‡] Brittany D. Jenkins,^c Rui Cheng,^b Bryana N. Harris,^d Weizhong Zhang,^a Jin Xie,^a Jonathan R. Murrow,^e Jamie Hodgson,^f Mary Egan,^f Ana Bankey,^f Petros G. Nikolinakos,^f Haythem Y. Ali,^g Kristina Meichner,^h Lisa A. Newman,^{ij} Melissa B. Davis^{*cjk} and Leidong Mao^{‡*b}

Isolation of circulating tumor cells (CTCs) from blood provides a minimally-invasive alternative for basic understanding, diagnosis, and prognosis of metastatic cancer. The roles and clinical values of CTCs are under intensive investigation, yet most studies are limited by technical challenges in the comprehensive enrichment of intact and viable CTCs with minimal white blood cell (WBC) contamination. Here, we report a novel method based on contrast of cell magnetization in biocompatible ferrofluids (a colloidal magnetic nanoparticle suspension), termed as integrated ferrohydrodynamic cell separation (iFCS), that enriches CTCs in a tumor antigen-independent and cell size variation-inclusive manner, achieves a high throughput (12 mL h⁻¹), high recovery rate (99.08% at down to ~10 cells per mL spike ratio), and low WBC contamination (533 cells for every one milliliter blood processed) and is biocompatible. This method will enable large cohort research to define the clinical and diagnostic value of CTC subtypes.

Received 28th February 2019,
Accepted 16th April 2019

DOI: 10.1039/c9lc00210c

rsc.li/loc

Introduction

Insights into heterogeneity among circulating tumor cells (CTCs) have significant implications for basic and translational research of metastatic cancer that is responsible for over 90% of cancer-related mortality.^{1–4} While primary tumor characterization is the most common source of material to predict tumorigenesis, clinically relevant findings would include the ability to predict whether the tumor will likely me-

tastasize and establish lethal colonies of tumors in distal organ sites. Due to the inherent heterogeneous composition of primary tumors, needle-biopsies and surgical samples may miss key diagnostic markers that would define the metastatic potential of the tumor. Characterizing blood borne circulating tumor cells provides a window into metastasis research as tumor cells are in route to their new niche, where these cells represent the disease potential of the tumors to establish multiple sites.^{3,4} Hence, CTCs could be a more representative sample of tumor disease potential than a primary tumor biopsy, including a compendium of genetic changes that increase metastatic potential over the course of tumor evolution. Development of innovative technologies that will allow the enrichment and characterization of a complete repertoire of viable CTCs could increase our understanding of metastasis and may lead to novel applications including the creation of *in vitro* and *ex vivo* models to experimentally manipulate and screen panels of patient-derived tumors.

Three concurrent technical challenges in existing CTC enrichment methods, including the dependence on specific tumor antigens for tumor cell recognition, inability to account for the variation of tumor cell sizes in isolation, and difficulty in keeping CTCs viable and intact for downstream analysis, complicated the study and applications of CTCs. These issues are worsened by the fact that CTCs are extremely rare, estimated at less than 10 tumor cells in every one-milliliter of whole blood. Past studies have shown that CTCs isolated by

^a Department of Chemistry, The University of Georgia, Athens, GA 30602, USA

^b School of Electrical and Computer Engineering, The University of Georgia, Athens, GA 30602, USA. E-mail: mao@uga.edu

^c Department of Genetics, The University of Georgia, Athens, GA 30602, USA

^d Department of Chemical Engineering, Auburn University, Auburn, AL 36830, USA

^e Department of Medicine, Augusta University–The University of Georgia Medical Partnership, Athens, GA 30602, USA

^f University Cancer & Blood Center, LLC, Athens, GA, 30607, USA

^g Department of Hematology and Oncology, Henry Ford Health System, Detroit, MI 48202, USA

^h Department of Pathology, College of Veterinary Medicine, The University of Georgia, Athens, GA 30602, USA

ⁱ Department of Surgery, Henry Ford Health System, Detroit, MI 48202, USA

^j Department of Surgery, Weill Cornell Medicine, New York, NY 10021, USA. E-mail: mbd4001@med.cornell.edu

^k Department of Public Health Sciences, Henry Ford Health System and Henry Ford Cancer Institute, Detroit, MI 48202, USA

† Electronic supplementary information (ESI) available. See DOI: 10.1039/c9lc00210c

‡ These authors contributed equally: Wujun Zhao and Yang Liu.

the US Food and Drug Administration (FDA) approved CellSearch system, identified by the epithelial cell adhesion molecule (EpCAM) alone, were associated with poor prognosis in metastatic and localized carcinomas in clinical trials.^{5,6} However, increasingly CTCs were found to be a rare and heterogeneous population of different phenotypic subtypes,^{1,7} in which a fraction of original epithelial tumor cells could transition into stem-like mesenchymal cells in a metamorphosis noted as EMT, epithelial to mesenchymal transition.³ This transition may be what gives CTCs the traits of high motility, invasiveness and limitless potential to create a new tumor site; therefore cells that have gone through this transition could possess the greatest threat of metastasis and short-term recurrence.^{3,4} Given the importance of EMT CTCs, the influence of mesenchymal properties on the prolonged survival of CTCs in the circulation, and on their capacity to form metastatic tumors, new methods are urgently needed to allow for a comprehensive enrichment and analysis of viable CTCs.

Microfluidics-based methods have provided a new avenue to enrich and study CTCs for the past decade but were often biased because of the use of specific tumor antigens or cell size threshold in enrichment. The majority of microfluidic methods operated based on either marker-dependent or cell size-dependent principles.⁸ For example, marker-dependent methods that relied on EpCAM or other combinations of tumor cell surface antigens were rendered ineffective due to the inherent heterogeneity of tumor subtypes.⁹ The significant difference among various markers and their expression levels in CTCs undergoing EMT was difficult to predict, resulting in incomplete recovery of CTCs from clinical samples. Cell size-dependent methods including those based on filtration,¹⁰ Dean flow and vortex chip^{11,12} depleted blood cells and recovered CTCs that were larger than $\sim 10 \mu\text{m}$ in diameter, based on a presumed size difference between blood and cancer cells.⁸ The drawback of these methods was that a significant percentage of CTCs in circulation were comparable or even smaller than blood cells. For example, CTCs isolated by the CellSearch system showed a polydispersity of cellular diameters, with as small as $\sim 4 \mu\text{m}$ CTCs captured from patients with malignant carcinomas and from patients with metastatic breast cancer.^{13,14} Others reported that CTCs smaller than $\sim 6\text{--}8 \mu\text{m}$ (comparable to the red blood cell disk diameter) were captured using various methods from patients with prostate cancer, metastatic breast cancer, small cell lung cancer and metastatic colorectal cancer.^{15–20} In addition, our measurements of human white blood cells (WBCs) and cultured cancer cells revealed that there was a significant size overlap between the two, and an appreciable percentage (*e.g.*, $\sim 35\%$ for DMS79 and H69 small cell lung cancer cell lines) of cancer cells were smaller than $10 \mu\text{m}$. As a result, it was challenging for cell size-dependent methods to achieve complete recovery and low blood cell contamination simultaneously.^{8,21} Furthermore, CTCs are fragile and need to be processed with gentle enrichment conditions to keep their viability and tumorigenic capability for downstream studies. In

summary, the inherent bias in tumor antigen-dependent and cell size-dependent methods, and the recognition that CTCs are highly rare, heterogeneous and fragile highlight the need to develop new methods that can enrich viable CTCs regardless of their surface antigen and size profiles.

In this paper, we addressed the above-mentioned challenges through the development of a novel CTC enrichment method that is based on the contrast of cell magnetization in ferrofluids, termed as integrated ferrohydrodynamic cell separation (iFCS). iFCS integrated both “diamagnetophoresis” and “magnetophoresis” of cells in a biocompatible ferrofluid with tunable magnetic nanoparticle concentration in a microfluidic device. The magnetization of the ferrofluid was chosen to lie between that of WBCs and CTCs, so that WBCs (labeled with magnetic beads) possessed a higher magnetization than their surrounding ferrofluids, and therefore flowed to a different device outlet than CTCs, which were unlabeled and possessed a lower magnetization (almost zero) than ferrofluids. Ferrofluids acted as liquid “magnetization filters”, which enriched CTCs with almost zero magnetization and depleted WBCs with high magnetization. The detailed description of the method is depicted in the Results and discussion section. Cell separation using either “diamagnetophoresis” or “magnetophoresis” alone is not new and has been summarized in recent reviews.^{22–27} However, demonstrations of co-existing “diamagnetophoresis” and “magnetophoresis” in microfluidic devices are new and limited only in microbead manipulation in the literature.^{28,29} Here we applied this method in a challenging CTC problem and achieved tumor antigen-independent and cell size variation-inclusive enrichment; it allows for simultaneous depletion of WBCs and enrichment of viable CTCs, resulting in complete recovery of intact and viable CTCs with minimal WBC contamination that were suitable for clinical applications.

In developing this method, we performed systematic parametric studies of key factors influencing the performance of iFCS and determined parameters for the high throughput (12 mL h^{-1}), high recovery rate (99.08% at down to ~ 10 cells per mL spike ratio), low WBC contamination (533 cells for every one milliliter blood processed) and biocompatible enrichment (cell viability of $97.69 \pm 0.70\%$ after enrichment) of CTCs from the blood of cancer patients. iFCS was first validated with cancer cells from 8 cultured cell lines of 3 different types of cancer. The mean recovery rate of cancer cells from red blood cell (RBC)-lysed blood using this method was 99.08%. The prototype iFCS device carried over on average 533 ± 34 WBCs per mL of blood processed. Enriched cancer cells had excellent short-term viability and intact capability to proliferate to confluence. Clinically, iFCS was first used to study cell size variation and surface antigen expression heterogeneity of CTCs enriched from 3 breast cancer patients and 3 lung cancer patients. This study revealed a high degree of variation in CTC sizes. 55.4% of patient-derived CTCs possessed an effective diameter of less than $10 \mu\text{m}$, and there was a significant overlap in sizes between CTCs and WBCs. This study also showed the heterogeneity of epithelial and

mesenchymal characteristics in patient CTCs' surface antigen expression. These results highlighted the need for tumor antigen-independent and cell size variation-inclusive methods such as iFCS. We used iFCS at a remote site (Henry Ford Health System, Detroit, Michigan) to investigate whether variable counts of CTC subtypes would correlate with clinical and diagnostic variables. We found, within a small cohort ($n = 6$) of early stage breast cancer patients, that mesenchymal and EMT subtypes of CTCs had a higher correlation to tumor grade than epithelial subtype.

Experimental section

Model of iFCS and its validation

We developed an analytical model used in this study to simulate cell trajectories in ferrofluids in a three-dimensional (3D) manner.^{30,31} It could predict 3D transport of diamagnetic cancer cells and magnetic WBCs in ferrofluids inside a microfluidic channel coupled with arbitrary configurations of permanent magnets. The magnets produced a spatially non-uniform magnetic field that led to a magnetic force on the cells. The trajectories of the cells in the device were obtained by (1) calculating the 3D magnetic force *via* an experimentally verified and analytical distribution of magnetic fields as well as their gradients, together with a nonlinear Langevin magnetization model of the ferrofluid and (2) solving the governing equations of motion using analytical expressions of magnetic force and hydrodynamic viscous drag force in MATLAB (MathWorks Inc., Natick, MA).

Synthesis and characterization of ferrofluids

Maghemite nanoparticles (10.91 ± 4.86 nm) were synthesized by a chemical co-precipitation method as previously described.³⁰ The size and morphology of maghemite nanoparticles were characterized *via* transmission electron microscopy (TEM; FEI, Eindhoven, the Netherlands). The magnetic properties of the ferrofluid were measured at room temperature using a vibrating sample magnetometer (VSM; MicroSense, Lowell, MA). The viscosity of ferrofluids was characterized with a compact rheometer (Anton Paar, Ashland, VA) at room temperature. Ferrofluid characterization data are listed in Fig. S1.†

Cell culture and sample preparation

Cancer cell lines (ATCC, Manassas, VA) including four breast cancer (BrC) cell lines (HCC1806, HCC70, MCF7 and MDA-MB-231), two non-small cell lung cancer (NSCLC) cell lines (H1299 and H3122), two small cell lung cancer (SCLC) cell lines (DMS79 and H69), and one prostate cancer cell line (PC-3) were used in this study. The cell lines were cultured following the manufacturer's recommended protocol. Cancer cells were fluorescently stained with CellTracker Green (Life Technologies, Carlsbad, CA) before each use. Cells were counted with a Nageotte counting chamber (Hausser Scientific, Horsham, PA) to determine the exact number of cells

per μL . Desired cancer cells (10, 25, 50, 100 or 200) were spiked into 1 mL of labeled WBCs.

Ferrofluid biocompatibility

Short-term cell viability after iFCS was examined using a Live/Dead assay (Life Technologies, Carlsbad, CA). For long-term proliferation, separated HCC1806 cells from an iFCS device were washed three times with culture medium to remove the nanoparticles, and then the cells were suspended in culture medium and seeded into a T25 flask. The cells were then cultured at 37 °C under a humidified atmosphere of 5% CO_2 . Cellular morphology was inspected every 24 hours.

iFCS device fabrication and assembly

Microfluidic devices were made of polydimethylsiloxane (PDMS) using standard soft lithography techniques. The thickness of the microfluidic channel was measured to be 300 μm by a profilometer (Veeco Instruments, Chadds Ford, PA). The device was placed within a custom aluminum manifold that held four NdFeB permanent magnets (K&J Magnetics, Pipersville, PA) in a quadrupole configuration. Each magnet was 50.8 mm in length, 6.35 mm in both width and thickness, and had a remanent magnetization of 1.48 T.

Microfluidic experimental setup and procedure

During a typical experiment, a microfluidic device inserted within the manifold was placed on the stage of an inverted microscope (Axio Observer, Carl Zeiss, Germany) for observation and recording. Two fluid inputs were controlled by individual syringe pumps (Chemyx, Stafford, TX). Blood samples were injected into an inlet of an iFCS device, and a sheath flow of ferrofluids was injected into a second inlet. Images and videos of cells were recorded with a CCD camera (Carl Zeiss, Germany). After enrichment, cells were collected in a 15 mL centrifuge tube with complete culture medium. Fabricated devices were flushed with 70% ethanol for 10 minutes and then primed with 1 \times phosphate-buffered saline (PBS) supplemented with 0.5% (w/v) bovine serum albumin (BSA) and 2 mM EDTA (Thermo Fisher Scientific, Waltham, MA) for 10 minutes before each use.

Human subject statement and sample processing

All experiments related to human subjects were performed in compliance with the applicable federal, state, and institutional policies and procedures in the United States. The names of the institutional committees that approved these experiments are listed below. Informed consent was obtained for any experimentation with human subjects. Healthy human blood samples were obtained from the Clinical and Translational Research Unit of the University of Georgia with informed consents according to a protocol approved by the University of Georgia Institutional Review Board (IRB) (STUDY00005431). Healthy donor samples were used for spike-in experiments with cell lines. Cancer patient samples

collected at the University Cancer and Blood Center (Athens, Georgia) were approved by the University of Georgia Institutional Review Board (IRB) (STUDY00005431) before study initiation and informed consent was obtained from the participants. Cancer patient samples collected at Henry Ford Health System (Detroit, Michigan) were approved by the Henry Ford Health System Institutional Review Board (IRB) (Davis-11564) before study initiation and informed consent was obtained from the participants. All blood samples were collected in either vacutainer K₂-EDTA tubes (BD, Franklin Lakes, NJ) or cell-free DNA BCT (Streck, Omaha, NE) and were processed within 2 hours of blood draw. Detailed patient information and CTC enumeration are listed in Table S1.† Complete blood count (CBC) reports were obtained to determine the number of WBCs. Whole blood was labeled with leukocyte-specific biotinylated antibodies including anti-CD45 (eBioscience, San Diego, CA), anti-CD16 (eBioscience, San Diego, CA), and anti-CD66b (BioLegend, San Diego, CA) for 30 minutes. The antibody conjugated blood was lysed with RBC lysis buffer (eBioscience, San Diego, CA) for 5 minutes at room temperature. Fig. S2† shows that RBC lysis resulted in a small but negligible cell loss (0.08%). Blood cells were then incubated with streptavidin-coated magnetic Dynabeads (Life Technologies, Carlsbad, CA) for 30 minutes on a rocker. All the labeling and washing procedures were carried out following the manufacturer's recommended protocol. Blood cells were finally suspended in the same volume of ferrofluid (0.028% v/v) containing 0.1% (v/v) Pluronic F-68 non-ionic surfactant (Thermo Fisher Scientific, Waltham, MA) before processing.

CTC identification

After processing of blood with an iFCS device, cells were immobilized onto a poly-L-lysine coated glass slide with a customized cell collection chamber. The collected cells were fixed with 4% (w/v) paraformaldehyde for 10 minutes and subsequently permeabilized with 0.1% (v/v) Triton X-100 in PBS for 10 minutes. The cells were then blocked with a blocking reagent (Santa Cruz Biotechnology, Dallas, TX) for 30 minutes. After blocking nonspecific binding sites, the cells were immunostained with primary antibodies including anti-cytokeratin (CK3-6H5)-FITC (Miltenyi Biotec, Auburn, CA) or EpCAM (EBA-1)-Alexa Fluor 488 (Santa Cruz Biotechnology, Dallas, TX), vimentin (V9)-Alexa Fluor 647 (Santa Cruz Biotechnology, Dallas, TX), and N-cadherin (13A9)-Alexa Fluor 594. Nuclei were counterstained with DAPI. All samples were also stained with anti-CD45 (HI30)-PE (BD Biosciences, San Jose, CA) to identify leukocytes. After immunofluorescence staining, the cells were washed with PBS and coverslipped with mounting medium for imaging or stored at 4 °C.

CTC culture

Primary cells were centrifuged at 200 × *g* for 5 minutes at 37 °C and resuspended in RPMI-1640 medium with 15% fetal bovine serum (FBS). Cells were cultured in a vented T25 flask at 37 °C with 5% CO₂. Primary cells were cultured over

a 72 hour period. At the end of the culture period, cultured cells were confirmed to have either an epithelial marker (EpCAM), or a mesenchymal marker (Vimentin), or both through immunofluorescent staining. Once confirmed, bright field images of cell culture were taken to calculate the primary cell growth rate over a 72 hour period.

Results and discussion

Overview of iFCS

The integrated ferrohydrodynamic cell separation (iFCS) method uses the following strategy to achieve tumor antigen-independent and cell size variation-inclusive enrichment of viable CTCs and simultaneous depletion of contaminating WBCs, leaving intact CTCs at its device's output with minimal WBC carryover. In this strategy, WBCs are rendered magnetic by labeling them with magnetic microbeads through a combination of leukocyte biomarkers, while CTCs remain unlabeled. WBC-bead conjugates and CTCs continuously flow through a microfluidic device filled with a ferrofluid, a colloidal suspension of magnetic nanoparticles with tunable particle concentration. The magnetization of the ferrofluid M_{fluid} , under an external magnetic field, is adjusted to be less than that of WBC-bead conjugates $M_{\text{WBC-bead}}$, so that unlabeled CTCs with a close to zero magnetization M_{CTC} , regardless of their sizes, are pushed towards a magnetic field minimum due to a phenomenon known as “diamagnetophoresis” (Fig. 1a, top),³² while WBC-bead conjugates are attracted to a magnetic field maximum through a competition between both “magnetophoresis” and “diamagnetophoresis” (Fig. 1a, bottom), and continuously depleted. In summary, the strategy of iFCS relies on the fact $M_{\text{CTC}} < M_{\text{fluid}} < M_{\text{WBC-bead}}$. It integrates both “diamagnetophoresis” and “magnetophoresis” of cells in ferrofluids to enrich the entire repertoire of CTCs from blood regardless of CTCs' surface antigen profile and size profile.

The iFCS-based CTC enrichment strategy relies on the establishment of both “magnetophoresis” and “diamagnetophoresis” of cells immersed in ferrofluids. A magnetic force is generated on magnetic or diamagnetic cells under a non-uniform magnetic field,³²

$$\vec{F}_{\text{mag}} = \mu_0 V_{\text{cell}} \left[(\vec{M}_{\text{cell}} - \vec{M}_{\text{fluid}}) \cdot \nabla \right] \vec{H} \quad (1)$$

where $\mu_0 = 4\pi \times 10^{-7} \text{ H m}^{-1}$ is the permeability of free space, V_{cell} is the volume of the cell, \vec{M}_{cell} is its magnetization, \vec{M}_{fluid} is magnetization of the ferrofluid surrounding the cell, and \vec{H} is magnetic field strength at the center of the cell. For cells in ferrofluids under a magnetic field, the magnitudes of the magnetization of the cell M_{cell} and the ferrofluid M_{fluid} with superparamagnetic particles in it can be modeled *via* a Langevin function. From eqn (1), we learn that the magnetic force directs cells to either a magnetic field maximum or minimum depending on the contrast between cell and fluid magnetizations, *i.e.*, the sign of the term $\vec{M}_{\text{cell}} - \vec{M}_{\text{fluid}}$, and

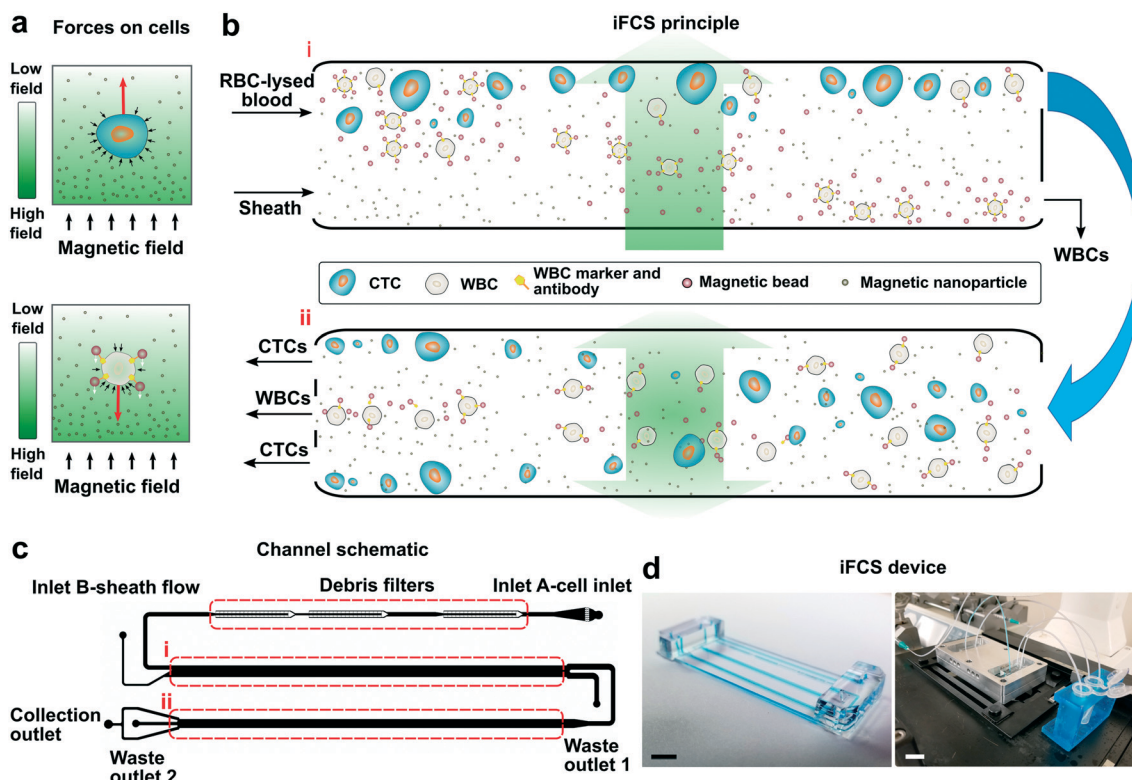


Fig. 1 Overview of an integrated ferrohydrodynamic cell separation (iFCS) system and its working principle. **a**. Top: Schematic of an unlabeled circulating tumor cell (CTC) experiencing “diamagnetophoresis” in a colloidal magnetic nanoparticle suspension (ferrofluid) and moving towards the minimum of a non-uniform magnetic field. Magnetization of the unlabeled CTCs M_{CTC} is near zero and less than their surrounding ferrofluids M_{fluid} . The diamagnetic body force on the cell is generated from magnetic nanoparticle induced pressure imbalance on the cell surface, and is proportional to the cell volume. Bottom: Schematic of a magnetic bead labeled white blood cell (WBC) experiencing both “diamagnetophoresis” from its cell surface and “magnetophoresis” from its attached beads in a ferrofluid and moving towards the maximum of a non-uniform magnetic field due to the fact that “magnetophoresis” outweighs “diamagnetophoresis”. The magnetization of the WBC-bead conjugates $M_{WBC-bead}$ is larger than their surrounding ferrofluid medium M_{fluid} . Color bar indicates the relative amplitude of the magnetic field. Red arrows show the direction of cell movement, small black arrows on the cell surface show the direction of magnetic nanoparticle induced surface pressure on cells, and white arrows show the magnetophoretic force on magnetic beads. **b**. Two enrichment stages were integrated into a single iFCS device to achieve cell size variation-inclusive and tumor antigen-independent enrichment of viable CTCs, and simultaneous depletion of contaminating WBCs. Prior to device processing, WBCs in blood were labeled with magnetic microbeads through leukocyte surface biomarkers so that the overall magnetization of the WBC-bead conjugates was larger than surrounding ferrofluids. The magnetization of the unlabeled CTCs was less than that of ferrofluids. In the first stage, a magnetic field gradient was generated to push unlabeled and sheath-focused CTCs to remain at the upper boundary of a microchannel, while attracting unbound magnetic microbeads and WBCs labeled with ≥ 3 microbeads towards a waste outlet. A significant percentage of magnetic beads and WBCs were depleted before the second stage to alleviate potential bead aggregation. In the second stage, a symmetric magnetic field with its maximum at the middle of the channel was used to attract the remaining WBC-bead conjugates towards the channel center for fast depletion, and direct unlabeled CTCs towards the upper and lower boundaries for collection. Green arrows with gradients indicate the distribution of magnetic fields in each stage. **c**. Top-view of the iFCS microchannel. The microchannel consists of a filter that removes larger than $\sim 50 \mu\text{m}$ debris, a first and second stage for CTC enrichment and WBC depletion. **d**. A photo of the prototype microchannel (left) and assembled iFCS device with four permanent magnets in a quadrupole configuration inside a holder (right). The microfluidic device and permanent magnets were placed within an aluminum manifold during its operation. Scale bars: 1 cm.

the magnitude of the force is also proportional to the volume of the cell V_{cell} .

Fig. 1 illustrates the design of a prototype iFCS microfluidic device based on the above principle. We incorporated two enrichment stages in prototype devices, in order to prevent magnetic microbead aggregation due to the use of a large number of magnetic beads. Prior to device processing, WBCs in blood were labeled with magnetic microbeads through leukocyte surface biomarkers so that the overall magnetization of the WBC-bead conjugates $M_{WBC-bead}$ was larger than the surrounding ferrofluid medium M_{fluid} . The

magnetization of the unlabeled CTCs M_{CTC} was close to zero and less than the surrounding ferrofluids M_{fluid} . In the first stage (Fig. 1b, top), a magnetic field was used to direct unlabeled and sheath-focused CTCs to remain at the upper boundary of a microchannel, while attracting unbound magnetic beads and WBCs labeled with ≥ 3 microbeads towards a waste outlet. This way, a significant percentage of beads and WBCs were depleted before the second stage, so that bead aggregation was minimized. In the second stage, a symmetric magnetic field with its maximum at the middle of the channel was used to attract the remaining WBC-bead conjugates

towards the channel center for fast depletion, while unlabeled CTCs flowing along the upper and lower channel boundaries were collected for analysis at the end of the channel (Fig. S3†). This design aimed to enrich all CTCs regardless of their surface antigens and sizes, and at the same time remove virtually all WBCs from collection outlets.

A physical model was developed to optimize the prototype device for practical CTC enrichment. CTCs are extremely rare in blood circulation and hidden among millions of WBCs with a similar size. The rate of CTC occurrence was reported to be <10 cells in one milliliter of blood.^{8,21} In order to optimize the iFCS method and objectively evaluate its performance, we used four metrics, including the cell-processing throughput, CTC recovery rate, WBC contamination and integrity of enriched cells, which were consistent with reports of existing methods (see Table S2†). For iFCS, the parameters that affected these four metrics include the device geometry, magnetic field and its gradient, magnetic bead labeling efficiency of WBCs, flow rate of cells, and ferrofluid properties. These parameters were coupled and needed to be optimized systematically. We created such a model that could predict three-dimensional (3D) trajectories of cells under laminar flow conditions inside the device.^{30,31} Diamagnetic force, magnetic force and hydrodynamic drag force were taken into consideration in simulating the cell trajectories. This physical model provided analytical and quick design optimization to determine the above-mentioned operating parameters depending on design constraints.

Optimization of iFCS for CTC enrichment

We optimized iFCS for tumor antigen-independent and cell size variation-inclusive enrichment of CTCs, with a goal of enriching the entire repertoire of viable CTCs with minimal WBC contamination. In quantitative terms, the performance goals for iFCS devices included: (1) a complete CTC recovery rate of >99% at a clinically relevant occurrence rate for CTCs (1–10 cells per mL), regardless of their surface antigens and sizes; (2) a minimal WBC contamination of ~500 cells at the device output for every one milliliter of blood processed; (3) a blood processing throughput of more than 10 mL h⁻¹; (4) unaffected cell integrity after enrichment, including viability and proliferation. These metrics were chosen as targets after a survey of existing microfluidic CTC enrichment methods (see Table S2†).

Systematic optimization of iFCS devices focused on the effects of device geometry, magnetic microbeads functionalized per WBC, magnetic field and its gradient, flow rates, and ferrofluid concentration on device performance, including the throughput, recovery rate and WBC contamination. Firstly, we determined microchannel dimensions for both stages by balancing a clinical need of processing at least 10 milliliters of blood within one hour, and a need to maintain laminar flow in the device. The final channel dimensions (first stage: 55 × 1.6 × 0.3 mm; second stage: 55 × 1.2 × 0.3 mm; $L \times W \times H$) were optimized so that the Reynold's number

was on the order of 10 when the cell flow rate was 12 mL h⁻¹, ensuring laminar flow conditions and physiologically equivalent shear rates (first stage average: 270.8 s⁻¹, range: 63.4–510.4 s⁻¹; second stage average: 190.8 s⁻¹; range: 54.4–360.5 s⁻¹) during CTC enrichment.³³ The prototype microchannel and assembled device are shown in Fig. 1c and d. Secondly, the amplitude of magnetic force on cells is proportional to the amplitude of the magnetic field gradient. In order to maximize the field gradient, we adopted a quadrupole magnet configuration in the iFCS device that could generate a magnetic flux density in the range of 0.5–1.5 T, and a magnetic flux density gradient up to 625 T m⁻¹ (Fig. 2a). Thirdly, the number of magnetic microbeads functionalized onto WBCs should be maximized to increase the contrast between WBC-bead conjugates and surrounding ferrofluids. Therefore, we optimized a WBC functionalization protocol by using a combination of three leukocyte surface biomarkers. Streptavidin-coated Dynabeads (1.05 μm, 11.4% Fe₂O₃ volume fraction) and biotinylated anti-human CD45, CD15 and CD66b antibody combinations were used. The results in Fig. 2b show that with antibody and bead concentrations (CD45: 100 fg per WBC, CD15: 75 fg per WBC, CD66b: 75 fg per WBC, magnetic beads: 125 per WBC), WBCs were conjugated with 34 ± 11 beads, and >99.9% of WBCs were labeled. The average magnetic content volume fraction of WBCs from the bead conjugation was 0.36%, with a minimal value of 0.026%, corresponding to WBCs that were labeled with just one magnetic bead. By choosing a ferrofluid concentration that was in the vicinity of the minimal value of WBCs' magnetic content volume fraction, it became possible to deplete virtually all WBCs.

The remaining optimization focused on the effect of ferrofluid concentration and cell-processing throughput on the performance metrics in the second stage. For this part of optimization, we calculated two outputs – a deflection in the y-direction for cells (see Fig. 2a for coordinates), denoted as Y , and a separation distance between WBCs and CTCs, denoted as ΔY . Both outputs were optimized using parameters including ferrofluid concentration (0–0.04% v/v) and throughput (0–700 μL min⁻¹, *i.e.*, 0–42 mL h⁻¹). The goal was to maximize the CTC recovery rate and minimize WBC contamination, which translated to maximizing ΔY and cell-processing throughput simultaneously. Fig. 2c shows that the separation distance ΔY reached a maximum when using a ferrofluid with a 0.028% magnetic volume fraction, and the largest throughput that could be achieved without compromising CTC recovery was 200 μL min⁻¹ (*i.e.*, 12 mL h⁻¹).

In summary, the optimization resulted in the following operating parameters for the prototype iFCS devices: a magnetic flux density in the range of 0.5–1.5 T, and a magnetic flux density gradient up to 625 T m⁻¹ *via* assembling four NdFeB permanent magnets in a quadrupole configuration; WBCs conjugated with 34 ± 11 magnetic beads, and over 99.9% WBCs labeled; a cell-processing throughput of 12 mL h⁻¹; a ferrofluid concentration of 0.028% (v/v). The microchannels in the device had a thickness of 300 μm and a total length of 55 mm, and the widths of the microchannels for

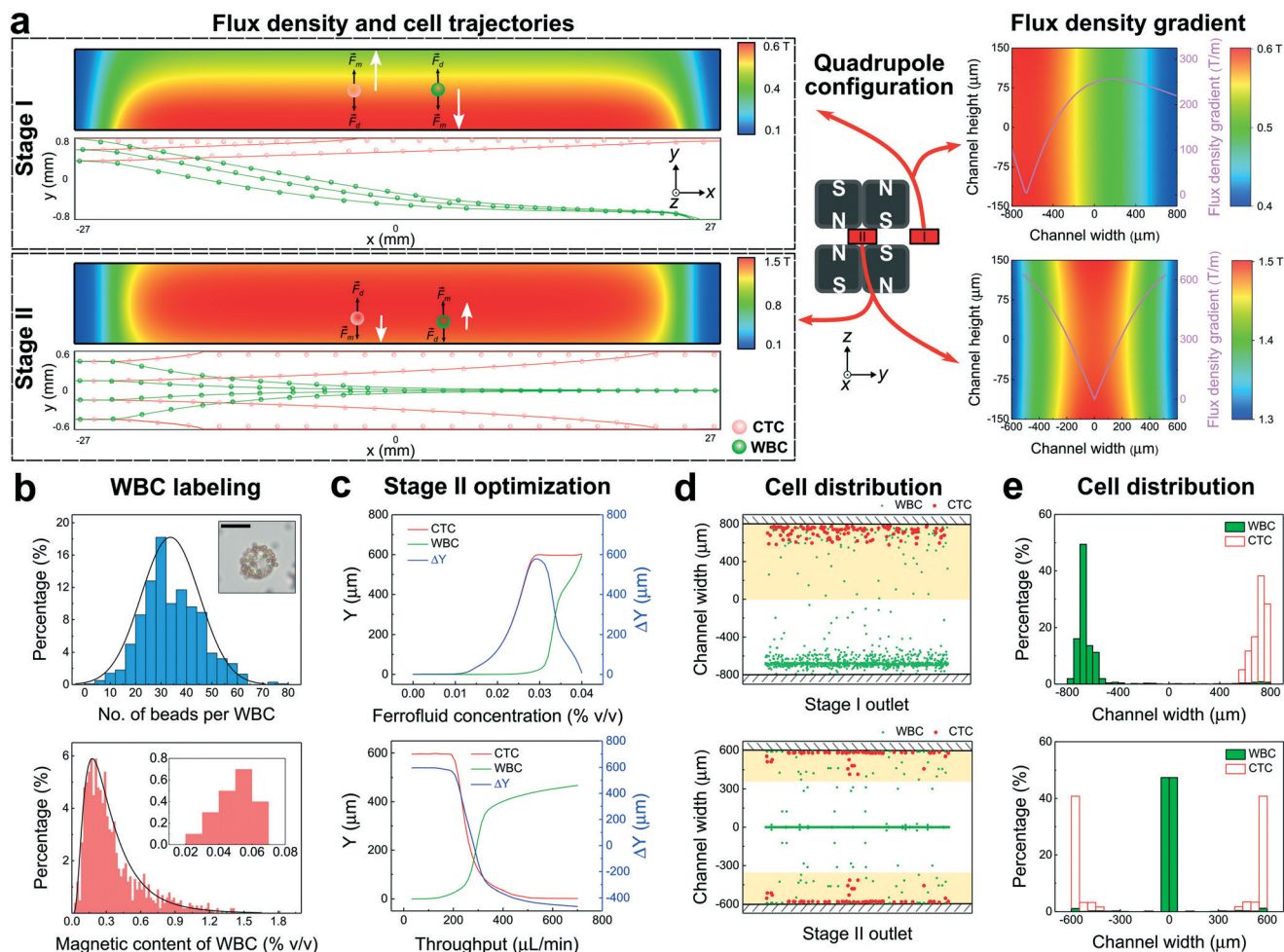


Fig. 2 System optimizations of prototype iFCS devices for high recovery (>99%) of viable and rare CTCs (down to ~10 cells per mL) with low WBC contamination (~500 cells per mL) at 12 mL h^{-1} throughput. **a.** Optimization of the magnetic flux density and its gradient in microchannels. Using four permanent magnets in a quadrupole configuration shown here, a maximal flux density of up to 0.6 T in the first stage (top), and up to 1.5 T in the second stage (bottom) in the x - y plane ($z = 0$) were obtained. Cell trajectories show that in the first stage WBCs (11.7 μm in diameter) labeled with ≥ 3 beads and unbound magnetic beads were continuously depleted into a waste outlet, while CTCs (15 μm in diameter) moved to the second stage. In the second stage, the remaining WBCs labeled with < 3 beads were further depleted, leaving CTCs at both upper and lower channel walls for collection. A cell flow rate of $200 \mu\text{L min}^{-1}$ was used for simulation. A maximal magnetic flux density gradient of 256 T m^{-1} in the first stage (top) and 625 T m^{-1} in the second stage (bottom) in the y - z plane ($x = 0$) were obtained. Schematic of magnetic (\vec{F}_m) and hydrodynamic drag (\vec{F}_d) forces on cells and their moving direction (white arrows; endpoints of white arrows indicating the equilibrium/final positions of cells) overlaid on top of magnetic flux density plots. **b.** Optimization of magnetic bead functionalization of WBCs. Top: Distribution of the number of magnetic Dynabeads per WBC ($n = 1000$). On average, 34 ± 11 Dynabeads are conjugated onto a single WBC. The inset is a WBC labeled with multiple Dynabeads. Scale bar: $10 \mu\text{m}$. Bottom: Magnetic content in labeled WBCs. More than 99.9% of WBCs are labeled with at least one bead, resulting in a 0.026% volume fraction of magnetic materials. This percentage value was used in subsequent optimization of ferrofluid concentration in order to minimize WBC contamination at the device's outlets. **c.** Optimizations of CTC recovery and WBC depletion (proportional to the separation distance ΔY) were conducted on parameters including the ferrofluid concentration (top) and device throughput (bottom). The optimal ferrofluid concentration is found to be 0.028%, while the optimal throughput to process a clinically relevant amount of blood is $200 \mu\text{L min}^{-1}$. In this optimization, the magnetic flux density and its gradient are the same as in **a**, and bead functionalization of WBCs is the same as in **b**. **d.** Visualization of CTC and WBC distributions at the end of microchannels in the first (top) and second (bottom) stages. CTCs were given a size range of 3–32 μm in diameter, while WBCs were given a size range of 5–25 μm in diameter. After the first stage, the majority of WBCs were depleted while all CTCs, regardless of their sizes, moved to the second stage. After the second stage, all CTCs were collected with a minimal amount of WBC contamination/carryover. Yellow areas indicate either the transfer channel to the second stage or the collection outlets, while white areas indicate waste outlets. **e.** Quantification of CTC and WBC distributions at the end of microchannels in the first (top) and second (bottom) stages. Results show that 96.35% of the initial WBCs were depleted after the first stage while all CTCs are preserved, including CTCs that are as small as 3 μm in diameter (top). After the second stage, 3.6% of the initial WBCs were further depleted and still all CTCs are preserved (bottom). Overall, after two stages, 99.95% of WBCs are depleted from the initial samples and all CTCs are preserved. Simulation parameters of **d** and **e** include: cell flow rate of $200 \mu\text{L min}^{-1}$, ferrofluid with concentration of 0.028%, magnetic flux density of 0.64 T and 1.5 T for stage I and stage II, and flux density gradient of 256 T m^{-1} and 625 T m^{-1} for stage I and stage II.

the first and second stages were $1600 \mu\text{m}$ and $1200 \mu\text{m}$, respectively. Using these parameters, we studied *via* simulation

the recovery rate of CTCs (CTC size range: 3–32 μm in spherical diameter) spiked into WBCs (WBC size range: 5–25 μm in

spherical diameter, 34 ± 11 magnetic beads per cell). We chose the smallest diameter of CTCs to be $3 \mu\text{m}$, a value that was smaller than the smallest reported CTCs from clinical samples,^{13,14} in order to test the robustness of the tumor antigen-independent and cell size variation-inclusive enrichment method. Fig. 2d shows a distribution of cell locations at the end of each stage. In quantitative terms, Fig. 2e reports that 96.35% of the initial WBCs that were labeled with ≥ 3 beads and all unbound beads were depleted after just the first stage while all CTCs were persevered, including the smallest $3 \mu\text{m}$ ones. After the second stage, 3.60% of the initial WBCs that were labeled with 2–3 beads were further removed without affecting CTCs. Overall, these two stages together were predicated to be able to deplete 99.95% of WBCs (corresponding to ~ 500 WBC contamination or carryover per milliliter of blood processed) and preserve 100% of CTCs regardless of their size profile.

Validation of iFCS with spiked cancer cells in human blood

Using the optimized device geometry and operating parameters, we studied cancer cell enrichment in iFCS prototype devices using a total of 8 cultured cancer cell lines that have drastically different average cell sizes and polydispersity, including 4 BrC cell lines, 2 NSCLC cell lines, and 2 SCLC cell lines. The performance of the enrichment was evaluated in terms of the cell-processing throughput, cell recovery rate, WBC contamination/carryover, and integrity of isolated cells. The results were also compared to simulation for testing the robustness of the analytical model. A typical enrichment process can be visualized in Fig. 3a and b, in which ~ 100 green fluorescently stained HCC1806 BrC cells (cell size range $6\text{--}47 \mu\text{m}$) were spiked into 1 mL of WBCs and processed in an iFCS device at a flow rate of 12 mL h^{-1} . In the first stage (Fig. 3a, top: phase contrast; bottom: epifluorescence), magnetic force attracted labeled WBCs and unbound beads toward a waste outlet while unlabeled cells including all CTCs and approximately 3.65% of WBCs were continuously flowed to the second stage. No aggregation of magnetic beads or ferrofluids was observed within one hour of operation. In the second stage (Fig. 3b, top: phase contrast; bottom: epifluorescence), magnetic forces deflected unlabeled cancer cells from the mixture toward both upper and lower collection outlets. Meanwhile, labeled WBCs were focused to the middle channel and depleted through a waste outlet.

We continued by testing the recovery rate and WBC carryover at cancer cell occurrence rates that were clinically relevant. The average rate of recovery for HCC70 BrC cells was 99.18% at spike ratios between 10 and 200 (10, 25, 50, 100, and 200) cells per mL and showed minimal variations among three repeats (Fig. 3c), which was consistent with simulation results. After cell enrichment, the device carried over on average 533 ± 34 WBCs per milliliter of blood processed. Much of the carryover was derived from WBCs that were either not labeled or labeled with just one magnetic bead (Fig. S4†), which was predicted by simulation results. The level of WBC

contamination found in iFCS devices was comparable to that of the monolithic version of the CTC-iChip (445 WBCs per mL of blood processed),³⁴ and lower than those of other recently reported methods, including magnetic ranking cytometry (~ 2000 WBCs per mL) and a previous version of the CTC-iChip ($\sim 32\,000$ WBCs per mL).^{7,35} After successfully demonstrating low-concentration cancer cell enrichment using the HCC70 BrC cell line, we expanded the characterization of the recovery rate in iFCS devices with 7 other types of cancer cell lines, including two SCLC cell lines. A measurement on the cell size of these cell lines and WBCs showed that there was a significant size overlap between WBCs and cancer cells, especially in the SCLC lines (Fig. 3d and Table S3†). A noticeable percentage of patient CTCs were smaller than $10 \mu\text{m}$ (55.4%; Fig. S5 and Table S5†). This would make the enrichment of cancer cells *via* size-dependent methods ineffective. However, as shown in Fig. 3e, by using the iFCS method, recovery rates of $98.46 \pm 0.50\%$, $99.05 \pm 0.75\%$, $99.35 \pm 0.46\%$, $99.40 \pm 0.85\%$, $99.13 \pm 0.49\%$, $99.11 \pm 1.25\%$, and $99.11 \pm 0.74\%$ were obtained for HCC1806 (BrC), MCF7 (BrC), MDA-MB-231 (BrC), H1299 (NSCLC), H3122 (NSCLC), DMS79 (SCLC), and H69 (SCLC) cell lines, respectively. The average recovery rate across 8 cancer cell lines was 99.16%. Taking into account the small cell loss (0.08%, see Fig. S2†) introduced by lysis, the average recovery rate across 8 cancer cell lines was 99.08%. This indicated a complete recovery of spiked cancer cells, including even the SCLC cells, regardless of their size profiles. The size distribution of three cell lines before and after enrichment in a single stage version of the iFCS device further confirmed that iFCS could enrich all cancer cells without a loss of small ones (Fig. 3f and Table S4†).

Ferrofluids and the iFCS enrichment process had little impact on cell viability and intactness, given the extremely low ferrofluid concentration (0.028% v/v) and low shear rate in enrichment. We examined the short-term cell viability and long-term cell proliferation of cancer cells following the enrichment process. As shown in Fig. 3g, the cell viability of HCC1806 BrC cells before and after enrichment was determined to be $98.30 \pm 0.56\%$ and $97.69 \pm 0.70\%$, respectively, indicating a negligible decrease in cell viability before and after the iFCS process. Representative fluorescence images of cells are shown in Fig. 3h. We also studied whether enriched cancer cells continued to proliferate normally. Fig. 3i shows the images of enriched HCC1806 BrC cells on the third day. They were able to proliferate to confluence and maintain the morphology after the iFCS process. The fluorescence image in Fig. 3i also confirmed that cells were viable after the 3 day culture. Enriched cells were intact and suitable for immunofluorescent and cytopathological staining (Fig. 3j and Fig. S6†).

Profiling cell size and surface antigen heterogeneity among CTCs in cancer patients

iFCS devices were capable of enriching CTCs regardless of their cell size variation and surface antigen heterogeneity

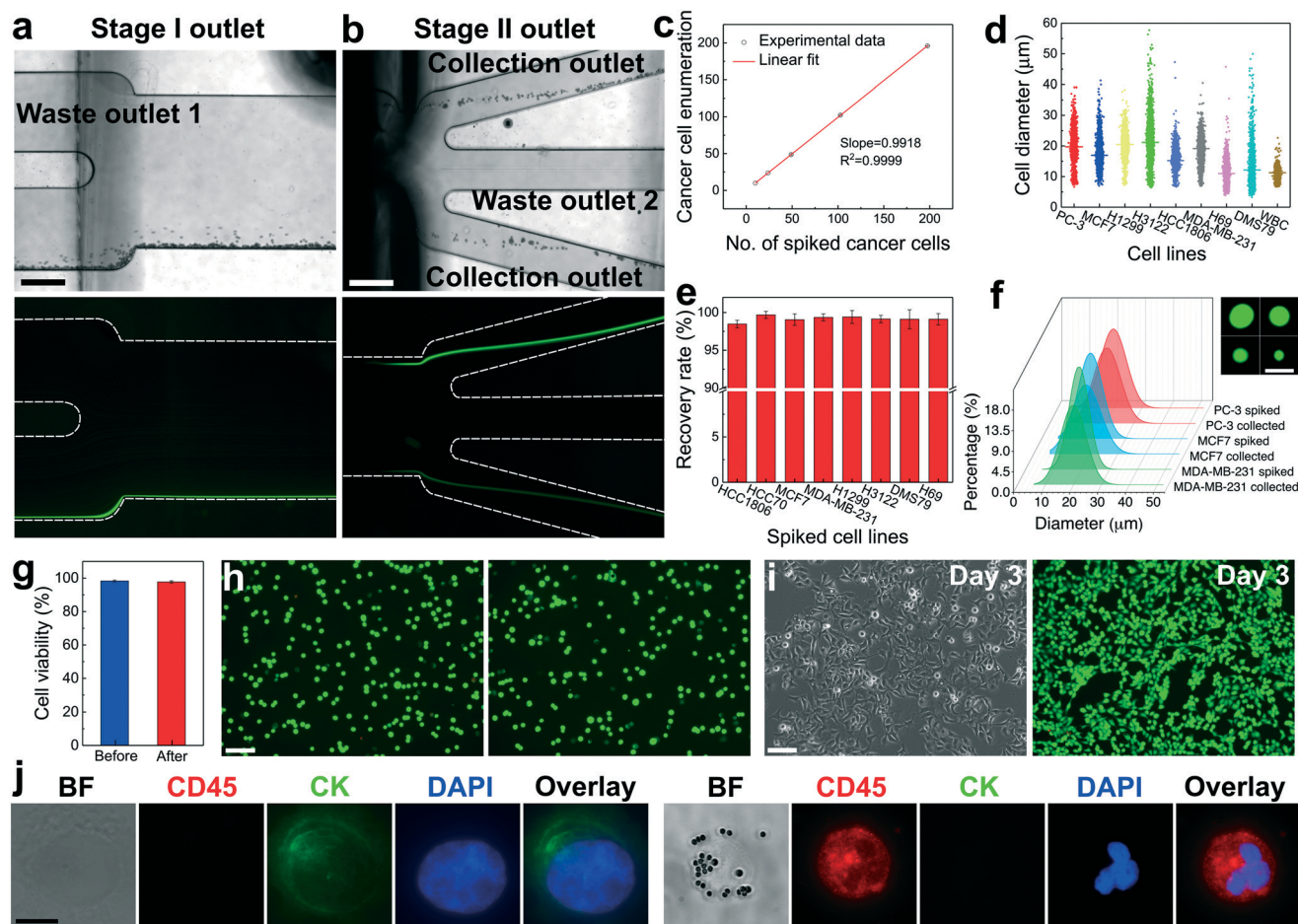


Fig. 3 Validation of prototype iFCS devices using cultured cancer cells spiked into WBCs, for over 99% of cancer cell recovery with minimal WBC contamination (~ 500 cells per mL) at a clinically relevant spike ratio (down to ~ 10 cells per mL) and throughput (12 mL h^{-1}). a. Visualization of cancer cell enrichment and WBC depletion (top: bright field; bottom: epifluorescence). In the first stage of the device, magnetic force attracted labeled WBCs and unbound beads toward waste outlet 1, while unlabeled cancer cells moved continuously into the second stage. Cancer cells were labeled with green fluorescence. Scale bar: $500 \mu\text{m}$. b. In the second stage, magnetic force deflected unlabeled cancer cells from the cell mixture toward the upper and lower collection outlets. At the same time, labeled WBCs were focused into the middle of the channel and depleted into waste outlet 2. Top: Bright field; bottom: epifluorescence. Scale bar: $500 \mu\text{m}$. Dashed lines in fluorescence images indicate the boundaries of the microchannel. c. Spike-in results from iFCS devices show high recovery (99.18%) of cancer cells. A series of spike-in enrichment experiments, in which a certain number (10, 25, 50, 100, and 200) of HCC70 breast cancer cells were spiked into 1 mL of labeled WBCs to emulate a clinically relevant CTC concentration at a cell-processing throughput of 12 mL h^{-1} . An average recovery rate of 99.18% was achieved ($R^2 = 0.9999$, $n = 3$). d. Size distribution of 8 cancer cell lines and WBCs. Both cancer cells and WBCs are polydispersed with overlapping sizes, highlighting the need for iFCS development to enrich CTCs in an antigen-independent and size inclusive manner. The mean diameter and standard deviations are listed in Table S3.† e. Recovery rates of spiked cancer cells (~ 100 cells per mL) from the cancer cell lines, including two small cell lung cancer (SCLC) lines, at a flow rate of 12 mL h^{-1} . Recovery rates of $98.46 \pm 0.50\%$, $99.68 \pm 0.46\%$, $99.05 \pm 0.75\%$, $99.35 \pm 0.46\%$, $99.40 \pm 0.85\%$, $99.13 \pm 0.49\%$, $99.11 \pm 1.25\%$, and $99.11 \pm 0.74\%$ were achieved for HCC1806, HCC70, MCF7, MDA-MB-231, H1299, H3122, DMS79 (SCLC), and H69 (SCLC) cell lines, respectively ($n = 3$). f. Size distribution of spiked and recovered cancer cells after the iFCS process, conducted in a single stage iFCS device. iFCS was able to preserve cancer cells of all sizes. The mean diameter and standard deviations of spiked and recovered cancer cells are listed in Table S4.† Inset: Recovered PC-3 prostate cancer cells showed polydispersity in diameters. The smallest recovered PC-3 cells had a diameter of $6.64 \mu\text{m}$. Scale bar: $20 \mu\text{m}$. g. Short-term cell viability comparison before and after the iFCS process. The cell viability of HCC1806 breast cancer cells before and after enrichment is determined to be $98.30 \pm 0.56\%$ and $97.69 \pm 0.70\%$, with little change. h. Representative images of Live/Dead staining before (left) and after (right) enrichment. Calcein AM (green, live cells) and EhD-1 (red, dead cells) channels were merged. Scale bar: $100 \mu\text{m}$. i. Representative images of cultured HCC1806 breast cancer cells after enrichment on the 3rd day. A Live/Dead staining of the cultured cells on day 3 shows excellent cell viability. Scale bar: $100 \mu\text{m}$. j. Immunofluorescence images of an intact spiked HCC1806 cancer cell (left panel) and an intact white blood cell conjugated with multiple magnetic beads (right panel). Three channels including CK (green), CD45 (red), and DAPI (blue) were used. Scale bar: $10 \mu\text{m}$. All error bars indicate s.d., $n = 3$.

from clinical samples of breast cancer patients. We investigated whether the heterogeneous population of CTC cell types enriched from iFCS could potentially yield greater clinical utility. For this purpose, we studied two cohorts of cancer

patients (breast cancer and lung cancer). We quantified the numbers and sizes of CTCs overall, then defined and quantified CTC subtypes in each patient and found distinct quantities of CTC subtypes within the patient cohort. We

categorized the CTC subtypes based on their expression of cell surface markers for epithelial and mesenchymal cell types.

In the first cohort, we used iFCS devices to process blood samples from 3 breast cancer patients who were recruited and consented from the University Cancer and Blood Center (Athens, Georgia) under an approved IRB protocol (University of Georgia, STUDY00005431). These patients are identified as the breast cancer optimization cohort (BrC-P#-Opt, in which # indicates the number of patient) in this paper. After iFCS enrichment, enriched cells were stained with the epithelial marker (EpCAM), mesenchymal markers (vimentin and N-

cadherin), leukocyte marker (CD45) and nucleus staining DAPI for their identification. CTCs were identified as epithelial positive (EpCAM+/CD45-/DAPI+), mesenchymal positive (Vim+/CD45-/DAPI+, N-cad+/CD45-/DAPI+ or Vim+/N-cad+/CD45-/DAPI+), or both epithelial and mesenchymal positive (EpCAM+/Vim+/N-cad+/CD45-/DAPI+), while WBCs were identified as CK-/Vim-/N-cad-/CD45+/DAPI+. The results from this study are summarized in Fig. 4. Examples of intact CTCs from device outputs are shown in Fig. 4a and Fig. S7a.† We first learned that the effective diameter of CTCs, defined as the maximum Feret diameter of cells from bright field images, showed a high degree of polydispersity among these

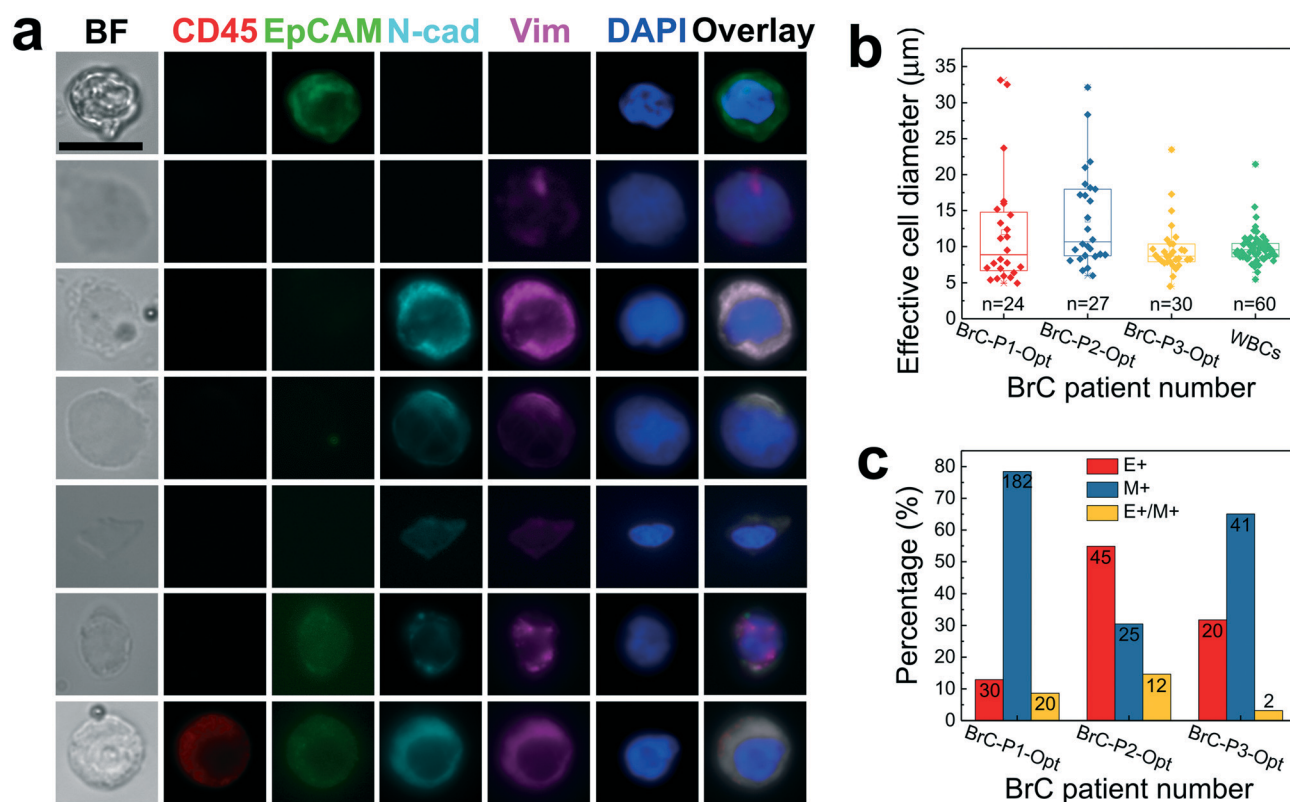


Fig. 4 Profiling variation in CTC sizes and heterogeneity of CTC surface antigen expressions from breast cancer patient samples (first cohort, $n = 3$). a. Bright field and immunofluorescence images of 7 selected individual CTCs enriched from 3 breast cancer (BrC) patients. Five channels were used in immunofluorescent staining, including the leukocyte marker CD45 (red), epithelial CTC marker EpCAM (green), mesenchymal CTC markers N-cadherin (N-cad, cyan) and vimentin (Vim, magenta), and nucleus marker DAPI (blue). White blood cells were identified as CD45+/EpCAM-/N-cad-/Vim-/DAPI+, while CTCs were identified as either EpCAM+/CD45-/DAPI+ (epithelial positive), or N-cad+/Vim+/CD45-/DAPI+ (mesenchymal positive), or EpCAM+/N-cad+/Vim+/CD45-/DAPI+ (both epithelial and mesenchymal positive). Scale bar: 10 µm. b. Quantitative analysis of the effective diameter (maximum Feret diameter of cells from their bright field images) of individual CTCs and WBCs enriched from 3 breast cancer patients' samples. Randomly selected CTCs from these patients revealed a high polydispersity of cell sizes. CTCs from patient 1 (breast cancer, stage IIIA, BrC-P1-Opt) had diameters of 11.99 ± 7.87 µm ($n = 24$; mean \pm s.d.; smallest 4.95 µm; largest 33.11 µm); CTCs from patient 2 (breast cancer, stage IA, BrC-P2-Opt) had diameters of 13.73 ± 6.76 µm ($n = 26$; mean \pm s.d.; smallest 6.00 µm; largest 32.10 µm); CTCs from patient 3 (breast cancer, stage IA, BrC-P3-Opt) had diameters of 9.67 ± 3.60 µm ($n = 30$; mean \pm s.d.; smallest 4.51 µm; largest 23.48 µm). WBCs pooled from 3 breast cancer patients had diameters of 9.83 ± 2.27 µm ($n = 60$; mean \pm s.d.; smallest 5.48 µm; largest 21.45 µm). c. Analysis of surface antigens expression of individual CTCs from 3 breast cancer patients' samples revealed a high heterogeneity of epithelial and mesenchymal characteristics in these cells. Cells from each patient are grouped into three categories (columns): epithelial positive (E+: EpCAM+/CD45-/DAPI+), mesenchymal positive (M+: N-cad+/Vim+/CD45-/DAPI+), and both epithelial and mesenchymal positive (E+/M+: EpCAM+/N-cad+/Vim+/CD45-/DAPI+). Numbers in each column indicate the absolute number of cells in each category. For BrC-P1-Opt, 12.93% of CTCs were epithelial positive, 78.45% of CTCs were mesenchymal positive, and 8.62% of CTCs were both epithelial and mesenchymal positive. For BrC-P2-Opt, 54.88% of CTCs were epithelial positive, 30.49% of CTCs were mesenchymal positive, and 14.63% of CTCs were both epithelial and mesenchymal positive. For BrC-P3-Opt, 31.75% of CTCs were epithelial positive, 65.08% of CTCs were mesenchymal positive, and 3.17% of CTCs were both epithelial and mesenchymal positive.

enriched cells. For example, patient 1 of this cohort (BrC-P1-Opt) had an advanced stage breast cancer diagnosis (stage IIIA, pre-surgery). We identified 232 CTCs in 9.0 mL of blood (25 CTCs per mL) from this patient. Effective diameters measured from randomly selected cells ($n = 24$) of this patient were $11.99 \pm 7.87 \mu\text{m}$ (mean \pm s.d.), where the smallest diameter was $4.95 \mu\text{m}$ and the largest was $33.11 \mu\text{m}$ (Fig. 4b). We characterized surface antigen expressions using the above mentioned markers for 232 cells from this patient. The characterization revealed a high degree of heterogeneity of antigen expressions: 12.93% was epithelial positive, 78.45% was mesenchymal positive, and 8.62% was both epithelial and mesenchymal positive (Fig. 4c). Patient 2 of this cohort (BrC-P2-Opt) had an early stage breast cancer diagnosis (stage IA, post-surgery). 82 CTCs were identified in 12.0 mL of blood (6 CTCs per mL) from this patient. Effective diameters of CTCs ($n = 26$) again showed high polydispersity (mean \pm s.d. = $13.73 \pm 6.76 \mu\text{m}$, smallest diameter $6.00 \mu\text{m}$, and largest diameter $32.10 \mu\text{m}$). Surface antigen expressions of cells ($n = 82$) revealed that 54.88% was epithelial positive, 30.49% was mesenchymal positive, and 14.63% was both epithelial and mesenchymal positive. Similarly, a third post-surgery patient (BrC-P3-Opt) with a stage IA breast cancer diagnosis exhibited variations in CTC size and heterogeneity among antigen expressions.

Overall, we found a variety of CTC subtypes that were positive for either epithelial or mesenchymal factors alone, or cells that were positive for both factors in this cohort (Fig. 4a). The cells that were positive for both factors likely represent CTCs that are in transition between epithelial and mesenchymal status, indicating their evolution to more virulent tumor cell phenotypes. We found that each patient had a wide range of sizes of CTCs that overlapped with the size distribution of WBCs (Fig. 4b). This indicates that existing cell-size dependent methods could greatly decrease the sensitivity of CTC enrichment, by excluding a large proportion of CTCs. Given the proportion of CTC subtypes in each patient, and the corresponding distribution of cell sizes for each patient, a large proportion of the size-excluded CTCs would have been mesenchymal (Fig. 4b and c). We also observed that the relative numbers of CTC types varied greatly among patients (Fig. 4c). For example, "Patient 1" (BrC-P1-Opt) and "Patient 3" (BrC-P3-Opt) carried predominantly mesenchymal CTCs and "Patient 2" (BrC-P2-Opt) carried predominantly epithelial CTCs. In each case, the relative number of transitioning EMT cells (positive for both epithelial and mesenchymal markers) was the least abundant within patient sample counts; however, the relative number of EMT cells significantly varied among patients. We went on to determine if these variable counts of CTC subtypes would correlate with clinical and diagnostic variables in a third cohort at Henry Ford Health System (Detroit, Michigan). Explicitly, we postulated whether the patients with the highest count of either mesenchymal or EMT cells would also have the most aggressive tumor phenotypes. These results will be discussed after the next section.

We extended our study to a second cohort consisting of 3 non-surgical stage IV lung cancer patients. They were recruited and consented from the University Cancer and Blood Center (Athens, Georgia) under the same IRB protocol (University of Georgia, STUDY00005431). These patients are identified as the lung cancer optimization cohort (LC-P#-Opt, in which # indicates the number of patient). The same blood collection, processing and cell identification approaches were used as those for the breast cancer cohort, except cytokeratin (CK) was replaced with EpCAM as the epithelial marker. CTCs were identified as epithelial positive (CK+/CD45-/DAPI+), mesenchymal positive (Vim+/CD45-/DAPI+, N-cad+/CD45-/DAPI+, or Vim+/N-cad+/CD45-/DAPI+), or both epithelial and mesenchymal positive (CK+/Vim+/N-cad+/CD45-/DAPI-), while WBCs were identified as CK-/Vim-/N-cad-/CD45+/DAPI+. The results are summarized in Fig. 5 with intact CTCs being shown in Fig. 5a and Fig. S7b.† We learned that CTCs from lung cancer patients were highly variable in cell sizes and antigen expressions too. For example, patient 1 of this cohort (LC-P1-Opt) was diagnosed with advanced stage non-small cell lung cancer (stage IV). 228 CTCs were identified in 9.0 mL of blood (25 CTCs per mL). Effective diameters of CTCs ($n = 39$) were $9.73 \pm 3.11 \mu\text{m}$ (mean \pm s.d.), where the smallest diameter was $4.59 \mu\text{m}$ and the largest was $18.52 \mu\text{m}$. Surface antigen expression characterization of cells ($n = 228$) showed that 11.84% was epithelial positive, 78.95% was mesenchymal positive, and 9.21% was both epithelial and mesenchymal positive. Data on the second patient (LC-P2-Opt, stage IV small cell lung cancer) and the third patient (LC-P3-Opt, stage IV non-small cell lung cancer) were consistent with this observation. The study on both breast cancer and lung cancer patients shows that CTCs from them are highly variable in cell diameters and in most cases their diameters overlap with contaminating WBCs (Fig. 4b and 5b). Furthermore, surface antigen expressions of CTCs are non-uniform across cells, making methods relying solely on the cell diameter or antigen expression ineffective. iFCS devices, insensitive to both size and antigen variations, are able to enrich CTCs and preserve these variations.

Non-EpCAM positive type of CTCs enriched by iFCS show better correlation with pathological variables in early-stage breast cancer patients

In the third cohort, we used iFCS devices at Henry Ford Health System (Detroit, Michigan) to process blood samples from 6 breast cancer patients who were recruited and consented there under an approved IRB protocol (Henry Ford Health System, Davis-11564). These patients are identified as the breast cancer culture cohort (BrC-P#-Culture, in which # indicates the number of patient). Peripheral blood was collected from the patients before initiation of treatment. Similar blood collection, processing and cell identification approaches were used to those in other cohorts. After iFCS enrichment, enriched cells were stained with the epithelial marker (EpCAM), mesenchymal markers (vimentin), and

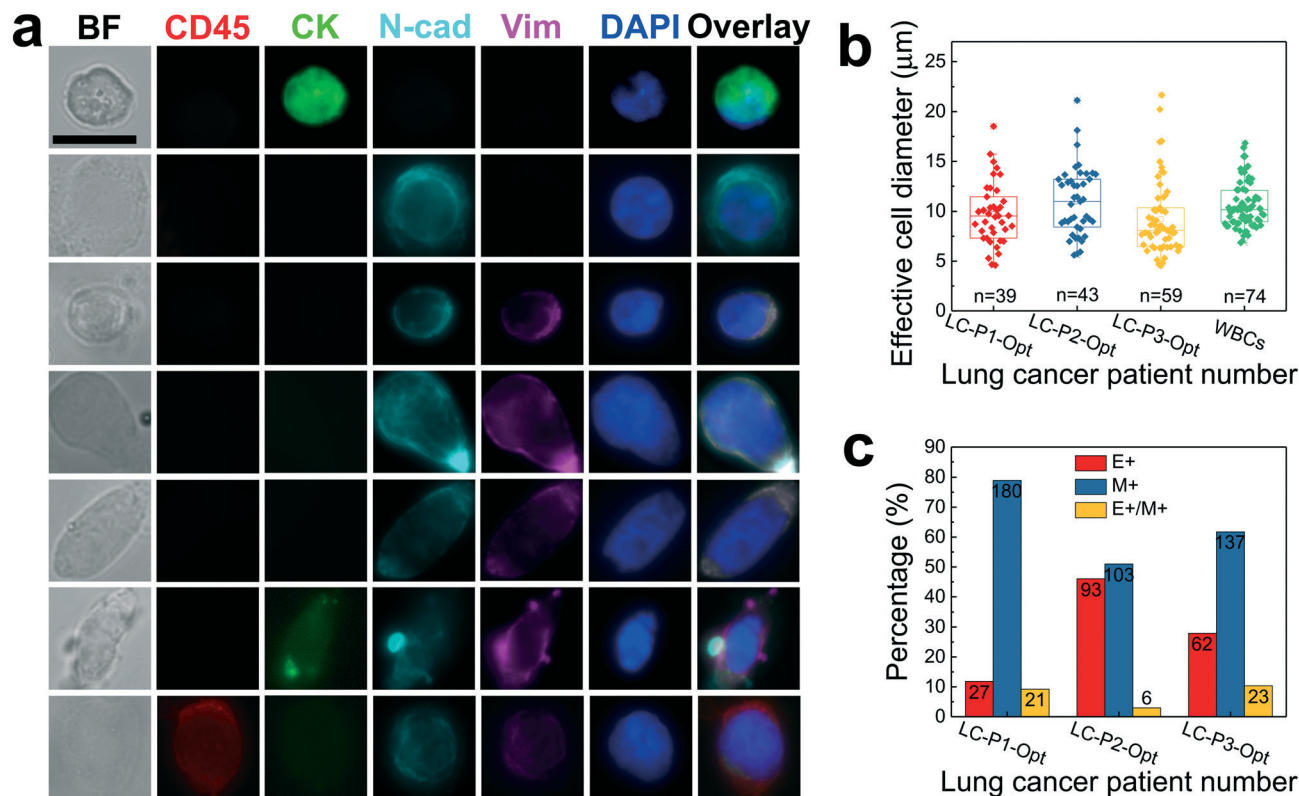


Fig. 5 Profiling variation in CTC sizes and heterogeneity of CTC surface antigen expressions from lung cancer patient samples (second cohort, $n = 3$). **a**. Bright field and immunofluorescence images of 7 selected individual CTCs enriched from 3 lung cancer (LC) patients. Five channels were used in immunofluorescent staining, including the leukocyte marker CD45 (red), epithelial CTC marker CK (green), mesenchymal CTC markers N-cadherin (N-cad, cyan) and vimentin (Vim, magenta), and nucleus marker DAPI (blue). White blood cells were identified as CD45+/CK-/N-cad-/Vim-/DAPI+, while CTCs were identified as either CK+/CD45-/DAPI+ (epithelial positive), or N-cad+/Vim+/CD45-/DAPI+ (mesenchymal positive), or CK+/N-cad+/Vim+/CD45-/DAPI+ (both epithelial and mesenchymal positive). Scale bar: 10 μm . **b**. Quantitative analysis of the effective diameter (maximum Feret diameter of cells from their bright field images) of individual CTCs and WBCs enriched from 3 lung cancer patients' samples. Randomly selected CTCs from these patients revealed a high polydispersity of cell sizes. CTCs from patient 1 (NSCLC, stage IV, LC-P1-Opt) had diameters of $9.73 \pm 3.11 \mu\text{m}$ ($n = 39$; mean \pm s.d.; smallest 4.59 μm ; largest 18.52 μm); CTCs from patient 2 (SCLC, stage IV, LC-P2-Opt) had diameters of $10.98 \pm 3.41 \mu\text{m}$ ($n = 43$; mean \pm s.d.; smallest 5.61 μm ; largest 21.13 μm); CTCs from patient 3 (SCLC, stage IV, LC-P3-Opt) had diameters of $9.23 \pm 3.67 \mu\text{m}$ ($n = 59$; mean \pm s.d.; smallest 4.55 μm ; largest 21.67 μm). WBCs from 3 lung cancer patients had diameters of $10.58 \pm 2.27 \mu\text{m}$ ($n = 74$; mean \pm s.d.; smallest 6.86 μm ; largest 16.83 μm). **c**. Analysis of surface antigen expression of individual CTCs from 3 lung cancer patients' samples revealed a high heterogeneity of epithelial and mesenchymal characteristics in these cells. Cells from each patient are grouped into three categories (columns): epithelial positive (E+: CK+/CD45-/DAPI+), mesenchymal positive (M+: N-cad+/Vim+/CD45-/DAPI+), and both epithelial and mesenchymal positive (E+/M+: CK+/N-cad+/Vim+/CD45-/DAPI+). Numbers in each column indicate the absolute number of cells in each category. For LC-P1-Opt, 11.84% of CTCs were epithelial positive, 78.95% of CTCs were mesenchymal positive, and 9.21% of CTCs were both epithelial and mesenchymal positive. For LC-P2-Opt, 46.04% of CTCs were epithelial positive, 50.99% of CTCs were mesenchymal positive, and 2.97% of CTCs were both epithelial and mesenchymal positive. For LC-P3-Opt, 27.93% of CTCs were epithelial positive, 61.71% of CTCs were mesenchymal positive, and 10.36% of CTCs were both epithelial and mesenchymal positive.

leukocyte marker (CD45) for their identification. CTCs were identified as epithelial positive (EpCAM+/CD45-), mesenchymal positive (Vim+/CD45-), or both epithelial and mesenchymal positive (EpCAM+/Vim+/CD45-), while WBCs were identified as CD45+. The results from this study are summarized in Fig. 6. When we compared the number of each CTC subtype with clinical-pathology variables, we found interesting correlations that suggest that the non-EpCAM positive type of CTCs, defined as vimentin-only positive and both EpCAM and vimentin positive, may have better prediction value with regard to prognosis and diagnosis, relative to epithelial (EpCAM-only positive) CTCs. Specifically, when we correlated the numbers of each CTC subtype with tumor grade, we

found that EpCAM-only CTCs were the least correlated with this variable ($R^2 = 0.025$) while mesenchymal cells (vimentin-only CTCs) were significantly more correlated ($R^2 = 0.584$). Interestingly, the EMT cells had the highest correlation with grade ($R^2 = 0.734$), suggesting that the presence of these transitioning cells may indicate the invasiveness and aggressiveness of the primary tumor (Fig. S8†).

We also investigated how relative CTC subtype counts correspond to standard clinical diagnostic variables. We observed that of the patients with the 21-gene recurrence risk scores (RS), the patient with the highest score (BrC-P6-Culture, RS = 16) had the highest proportion of mesenchymal only CTCs and also the lowest proportion of EMT CTCs. This

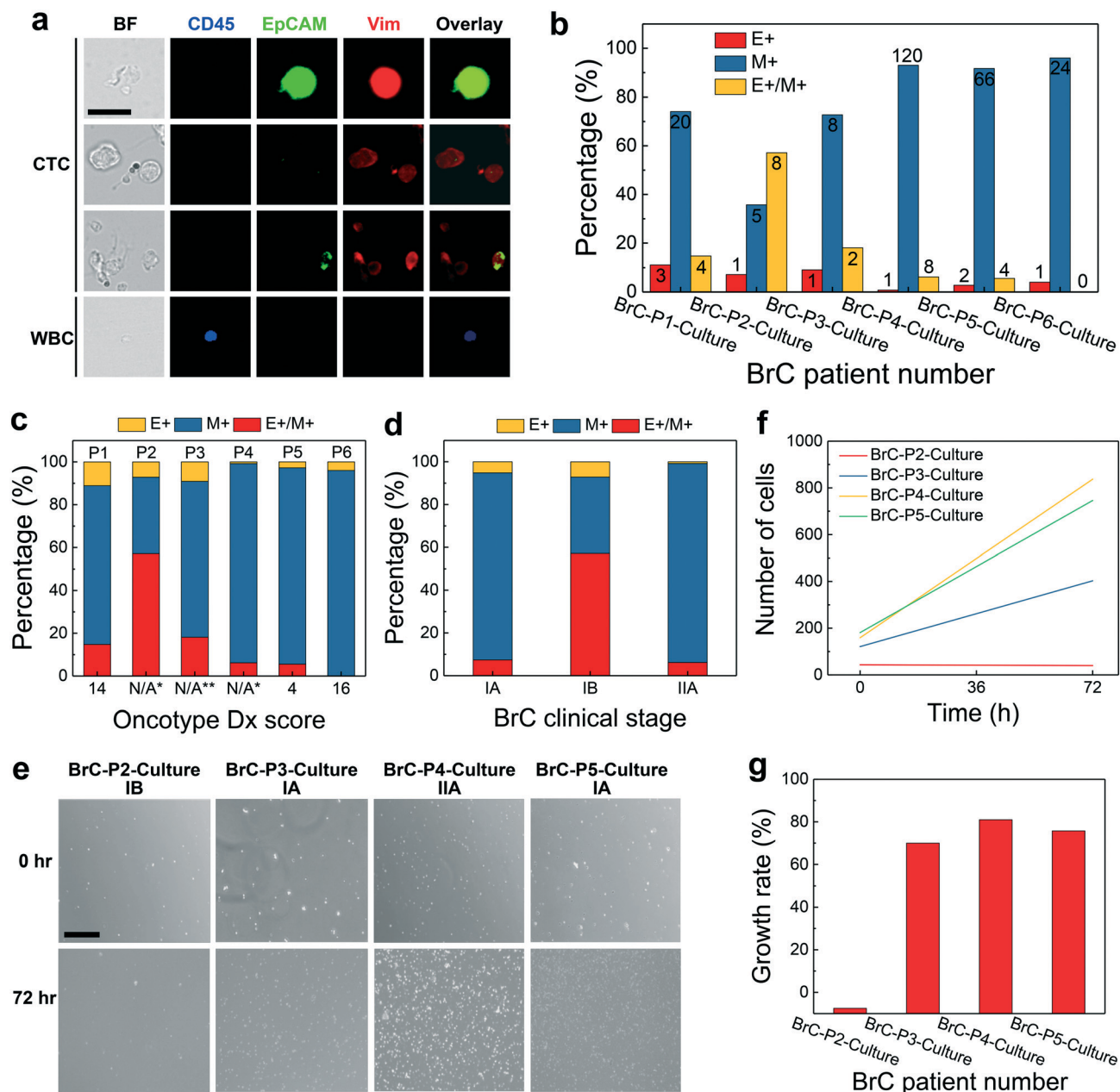


Fig. 6 Correlation between clinical stages, growth rates of CTC culture, Oncotype Dx scores and heterogeneity of CTC surface antigen expressions in early stage breast cancer patients (third cohort, $n = 6$). **a**. Bright field and immunofluorescence images of 3 representative CTCs and 1 WBC enriched from breast cancer patients. Cells were subjected to multiplexed immunofluorescence assessment with cell-type specific markers detected with distinct wavelength channels, including the leukocyte marker CD45 (blue), epithelial CTC marker EpCAM (green), and mesenchymal CTC marker vimentin (Vim, red). White blood cells were identified as CD45+/EpCAM-/Vim-, while CTCs were identified as EpCAM+/Vim-/CD45- (epithelial positive), EpCAM-/Vim+/CD45- (mesenchymal positive), or EpCAM+/Vim+/CD45- (both epithelial and mesenchymal positive). Scale bar: 10 μ m. **b**. Relative counts of CTC subtypes by surface antigen expression from 6 breast cancer patients' samples. Cells from each patient are grouped into three categories (columns): epithelial positive (E+: EpCAM+/Vim-/CD45-), mesenchymal positive (M+: EpCAM-/Vim+/CD45-), and both epithelial and mesenchymal positive (E+/M+: EpCAM+/Vim+/CD45-). Numbers in each column indicate the absolute number of cells in each category. **c**. Proportional components of CTC profiles for breast cancer patients, Oncotype Dx scoring indicated for each patient. Scores for P2, P3 and P4 patients are not available because their clinical stages are either too high (*confirmed metastasis) or too low (**non-invasive carcinoma/DCIS). **d**. The average proportional components of CTC subtypes are shown with respect to clinical staging. **e**. Representative images of primary cell culture of iFCS device output over a 72 hour period. NCCN staging for each BrC patient is represented next to the patient designation. Scale bar: 200 μ m. **f**. Combined total number of cells quantified from primary cell culture imaging for each BrC patient at 0 hours and the change in counts at 72 hours. **g**. Growth rate of cells in primary culture for each BrC patient ((cell number at 72 h - cell number at 0 h)/cell number at 72 h).

may indicate that the relative numbers of cells in transition vs. cells that have completely transitioned to mesenchymal

status may be indicative of metastatic potential. Conversely, the patient with the lowest RS score had the highest

proportion of epithelial CTCs and the largest proportion of EMT CTCs (Fig. 6c). Of all the patients with RS values in this cohort, when we compared these with the relative numbers of CTC subtypes, we found no significant correlation with this test. One limitation of this negative finding is that only 3 out of 6 patients had an indication for ordering the 21-gene recurrence test and therefore we could not determine a specific correlation of CTC subtypes with great confidence. As an alternative to recurrence risk scores, we investigated whether the relative correspondence of CTC subtypes with clinical stages had a better correlation in these patients with recurrence risk estimates. Similar to our 21-gene recurrence test observations, we found that the patient with the highest tumor stage (IIA) also had the highest proportion of mesenchymal-only CTCs and the lowest proportion of epithelial CTCs (Fig. 6d). While the limitations of these comparisons preclude statistical significance, there is a compelling trend of specific CTC subtypes correlated with the clinical stage and prognosis among the small subset of patients. These preliminary findings, while not yet clinically significant, clearly show the feasibility of utilizing the iFCS device output to establish basic research that can be translational upon further investigations and larger cohort numbers. Particularly, we hypothesize that our findings will be congruent with those already established with the correlated presence of CTCs and disease progression. Further, profiling subsets of CTCs can refine our understanding of specific mechanisms of metastasis that transcend the primary tumor site.

Because iFCS allows us to obtain viable cells, we also cultured CTCs for each patient as a pooled/bulk output initiation culture, as opposed to single-cell inoculation for homogeneous cultures of specific subtypes. CTC culturing has been documented to be a low-yield process with some methods focusing on long-term maintenance of primary CTCs for development of propagated cell lines using growth factor supplements.³⁶ Other studies focus on short-term colony cultures using growth factor cocktails or immune cell co-culture to study diversity in tumor phenotypes.^{37,38} Success rates of CTC culturing varied between <20 and 50%. In our CTC culturing protocol, primary cells were cultured in standard RPMI-1640 medium with 15% fetal bovine serum (FBS) over a 72 hour period simply to establish that the cell output was viable. At the end of the time course, cells were first confirmed to have either the epithelial marker (EpCAM), or mesenchymal marker (vimentin), or both through immunofluorescent staining (see Fig. S9†). Bright field images of each case's cell culture were then taken to calculate the cell growth rate. Ideally, confirmation of tumor origin would be utilized to verify the CTC integrity. However, for this pilot cohort, we were limited by resources and not able to carry out genetic testing. Nonetheless, with these cultures verified by epithelial and mesenchymal markers, we investigated the relative percentages of the CTC subtypes in each patient culture and measured the growth rate of the cultures over a 72 hour period. We had variable success with culture growth (Fig. 6e) and this corresponded to variable growth rates within cul-

tures that grew significantly (Fig. 6f). Of the patient samples that displayed significant growth curves (BrC-P3-Culture, BrC-P4-Culture, and BrC-P5-Culture) we found that their growth rate averaged over 60%. When we compared these growth rates with CTC subtype proportions, we found that the two patients with the highest growth curves had the lowest proportion of both epithelial and EMT CTCs, with the highest relative mesenchymal CTCs (of these successfully established cultures – patient BrC-P6-Culture had the highest mesenchymal proportion but the line was lost to contamination before a growth curve could be calculated). In a preliminary comparison, we observed that growth rates were positively correlated with the relative proportion of mesenchymal cells ($R^2 = 0.289$), though not significantly, and this finding suggests that the intended capture of viable CTCs has been accomplished with the iFCS device.

Comparison of iFCS to existing CTC enrichment methods

To objectively compare iFCS's performance to existing methods, we used four metrics including the cell-processing throughput, CTC recovery rate, WBC contamination and integrity of enriched cells. These metrics are often used in reports of existing methods. The performance metrics of iFCS were: (1) a recovery rate of 99.08% at an extremely low CTC occurrence rate (1–10 cells per mL); (2) a WBC carryover of 533 ± 34 cells for every 1 milliliter of blood processed; (3) a blood processing throughput of 12 mL h^{-1} ; (4) minimally affected cell integrity after enrichment. We compared iFCS's performance to a total of 36 recently published CTC enrichment methods (see Table S2†) and found that iFCS had better combinatorial performance in the above-mentioned four categories than all existing methods except for the CTC-iChip. We compared the performance of iFCS to the state-of-the-art CTC-iChip in Table S6.†^{34,35,39} iFCS and the CTC-iChip had similar performance metrics in the categories of throughput, WBC contamination and cell integrity. The operation of the CTC-iChip integrated three working principles including cell size based deterministic lateral displacement (DLD) to deplete red blood cells, inertial focusing to concentrate nucleated cells, and magnetophoretic separation to separate CTCs. The CTC-iChip had state-of-the-art performance in CTC enrichment and an advantage of whole-blood processing without the need for lysis. However, the size based DLD stage risked depleting CTCs smaller than or of similar size to red blood cells ($\sim 6\text{--}8 \mu\text{m}$), which appeared frequently in tumor antigen based enrichment methods.^{13–20} To the best of our knowledge, two generations of the CTC-iChip existed, with the original published in 2013 quoting its DLD cutoff size to be $8 \mu\text{m}$,³⁵ and a monolithic version published in 2017 quoting its DLD cutoff size to be $5.5 \mu\text{m}$.³⁴ Given that the disk diameter of a red blood cell is $6\text{--}8 \mu\text{m}$, it is reasonable to assume that the DLD stages in the CTC-iChip could not completely differentiate between red blood cells and CTCs of $6\text{--}8 \mu\text{m}$ or less in diameter, and risked depleting them all together. iFCS has an advantage of being able to

recover small CTCs, because it does not differentiate CTCs and blood cells based on their diameters. Instead it uses the contrast of cellular magnetization for enrichment. Two enrichment stages existed in prototype iFCS devices. In the first stage, unlabeled and sheath-focused CTCs were concentrated to the second stage, while WBCs labeled with multiple magnetic beads flowed to a waste outlet. In the second stage, WBCs were further depleted while unlabeled CTCs were collected. This design ensured that all CTCs were enriched regardless of their surface antigens and sizes, at the same time removing virtually all WBCs from collection outlets. We confirmed with patient samples that iFCS could recover small CTCs. On average, 34.5% of CTCs recovered by iFCS (33.1% for NSCLC CTCs, 36.4% for SCLC CTCs, and 34.6% for BrC CTCs) were less than 8 μm (see Table S5[†]). iFCS has a second advantage over the CTC-iChip for its simplicity in modeling and integration. A single physical model of iFCS, taking into account cellular diamagnetophoresis and magnetophoresis, provided analytical and quick design optimization and determined iFCS's operating parameters given design constraints. In contrast, the CTC-iChip operated on three entirely different working principles (DLD, inertial focusing and magnetophoresis), with each of them needing their own modeling and optimization process. The numbers of physical models required, as well as the complexity of integrating the devices together, could complicate the use and application of the CTC-iChip. Finally, we realize that the red blood cell lysis step in iFCS could potentially cause CTC loss in patient samples. Even though the cell loss was small (0.08%) in cancer cell line control experiments (see Fig. S2[†]), it is difficult to characterize such cell loss from patient samples without a side-by-side comparison between iFCS and a whole-blood processing technology such as the CTC-iChip. In summary, with other performance metrics (throughput, WBC contamination and cell integrity) being equal, iFCS has the advantages of recovering small CTCs, quick design and optimization processes, but lacks the ability to process whole blood in current devices.

Conclusions

We developed an iFCS method and its prototype devices for tumor antigen-independent and cell size variation-inclusive enrichment of CTCs from cancer patients. iFCS integrated both “diamagnetophoresis” and “magnetophoresis” of cells in a biocompatible ferrofluid with tunable magnetic nanoparticle concentration in a microfluidic device. The working principle was based on contrast of cell magnetization, with which ferrofluids acted as liquid “magnetization filters”.

CTCs with almost zero magnetization (less than that of ferrofluids) were enriched and WBCs with high magnetization (more than that of ferrofluids) were depleted. We developed an analytical model to guide the optimization processes of iFCS and determine appropriate operating parameters. Through validations with both spike-in samples and clinical samples using these operating parameters, the performance

of iFCS devices was determined to be: (1) a close-to-complete CTC recovery rate of 99.08% at a clinically relevant occurrence rate for CTCs (1–10 cells per mL), regardless of their surface antigens and sizes; (2) a minimal WBC contamination of 533 ± 34 cells at the device output for every one milliliter of blood processed; (3) a blood processing throughput of 12 mL h^{-1} ; (4) minimally affected cell integrity after enrichment, including viability and proliferation.

We used iFCS devices to investigate whether heterogeneous populations of CTC cell types could potentially yield clinical utility. From the first two cohorts of cancer patients (breast and lung cancers), we discovered a variety of CTC subtypes that were positive for epithelial or mesenchymal biomarkers alone, or cells that were positive for both markers. We also discovered that each patient had a high level of CTC size variation, which overlapped with the size distribution of WBCs. This finding highlights the need to develop a tumor cell antigen-independent and cell size variation-inclusive method for CTC studies.

Our third patient cohort – breast cancer cohort – in this study is limited to early-stage cancer patients that had no indication of metastatic disease. In this small cohort ($n = 6$), we found that EpCAM-only CTCs were the least correlated with tumor grade, mesenchymal cells (vimentin-only CTCs) were significantly more correlated, and EMT cells had the highest correlation, suggesting that the presence of transitioning EMT cells may indicate the invasiveness and aggressiveness of the primary tumor. We also attempted culturing of CTCs from these patients with variable success; 3 out of 6 patients' CTCs showed >60% growth over a 72 hour period. We found that the two patients with the highest CTC growth curves had the lowest proportion of both epithelial and EMT CTCs, and the highest relative mesenchymal CTCs. This suggests that the intended enrichment of viable CTCs has been validated with the iFCS device. We note that these results are from a small number of patients and are not yet clinically significant. Further investigations with large cohort numbers are needed in order to validate them.

Conflicts of interest

The University of Georgia filed patent protection for iFCS technology.

Acknowledgements

We express our gratitude to all patients and healthy donors who agreed to participate in this study. We also thank Kimberly Schmitz (Clinical and Translational Research Unit, University of Georgia) for her help in subject recruitment and coordination. This material is based upon work supported by the National Science Foundation under Grant No. 1150042 and 1659525, by the National Institute of General Medical Sciences of the National Institutes of Health under Award No. R21GM104528, and the National Center for Advancing Translational Sciences of the National Institutes of Health under

Award No. UL1TR002378. The content is solely the responsibility of the authors and does not necessarily represent the official views of the National Institutes of Health.

References

- M. Poudineh, E. H. Sargent, K. Pantel and S. O. Kelley, *Nat. Biomed. Eng.*, 2018, 2, 72–84.
- C. Alix-Panabieres and K. Pantel, *Nat. Biomed. Eng.*, 2017, 1, 0065.
- C. L. Chaffer and R. A. Weinberg, *Science*, 2011, 331, 1559–1564.
- A. W. Lambert, D. R. Pattabiraman and R. A. Weinberg, *Cell*, 2017, 168, 670–691.
- A. Romiti, S. Raffa, R. Di Rocco, M. Roberto, A. Milano, A. Zullo, L. Leone, D. Ranieri, F. Mazzetta, E. Medda, I. Sarcina, V. Barucca, C. D'Antonio, V. Durante, M. Ferri, M. R. Torrisi and P. Marchetti, *J. Gastrointest. Liver Dis.*, 2014, 23, 279–284.
- F. C. Bidard, D. J. Peeters, T. Fehm, F. Nole, R. Gisbert-Criado, D. Mavroudis, S. Grisanti, D. Generali, J. A. Garcia-Saenz, J. Stebbing, C. Caldas, P. Gazzaniga, L. Manso, R. Zamarchi, A. F. de Lascoiti, L. De Mattos-Arruda, M. Ignatiadis, R. Lebofsky, S. J. van Laere, F. Meier-Stiegen, M. T. Sandri, J. Vidal-Martinez, E. Politaki, F. Consoli, A. Bottini, E. Diaz-Rubio, J. Krell, S. J. Dawson, C. Raimondi, A. Rutten, W. Janni, E. Munzone, V. Caranana, S. A. Agelaki, C. Almici, L. Dirix, E. F. Solomayer, L. Zorzino, H. Johannes, J. S. Reis, K. Pantel, J. Y. Pierga and S. Michiels, *Lancet Oncol.*, 2014, 15, 406–414.
- M. Poudineh, P. Aldridge, S. Ahmed, B. J. Green, L. Kermanshah, V. Nguyen, C. Tu, R. M. Mohamadi, R. K. Nam, A. Hansen, S. S. Sridhar, A. Finelli, N. E. Fleshner, A. M. Joshua, E. H. Sargent and S. O. Kelley, *Nat. Nanotechnol.*, 2017, 12, 274–281.
- C. Alix-Panabieres and K. Pantel, *Nat. Rev. Cancer*, 2014, 14, 623–631.
- A. Dasgupta, A. R. Lim and C. M. Ghajar, *Mol. Oncol.*, 2017, 11, 40–61.
- H. K. Lin, S. Y. Zheng, A. J. Williams, M. Balic, S. Groshen, H. I. Scher, M. Fleisher, W. Stadler, R. H. Datar, Y. C. Tai and R. J. Cote, *Clin. Cancer Res.*, 2010, 16, 5011–5018.
- M. E. Warkiani, B. L. Khoo, L. D. Wu, A. K. P. Tay, A. A. S. Bhagat, J. Han and C. T. Lim, *Nat. Protoc.*, 2016, 11, 134–148.
- C. Renier, E. Pao, J. Che, H. E. Liu, C. A. Lemaire, M. Matsumoto, M. Triboulet, S. Srivinas, S. S. Jeffrey, M. Rettig, R. P. Kulkarni, D. Di Carlo and E. Sollier-Christen, *NPJ Precis. Oncol.*, 2017, 1, 15.
- W. J. Allard, J. Matera, M. C. Miller, M. Repollet, M. C. Connelly, C. Rao, A. G. J. Tibbe, J. W. Uhr and L. W. M. M. Terstappen, *Clin. Cancer Res.*, 2004, 10, 6897–6904.
- S. Riethdorf, H. Fritsche, V. Muller, T. Rau, C. Schindlbeck, B. Rack, W. Janni, C. Coith, K. Beck, F. Janicke, S. Jackson, T. Gornet, M. Cristofanilli and K. Pantel, *Clin. Cancer Res.*, 2007, 13, 920–928.
- J. J. Nieva and P. Kuhn, *Future Oncol.*, 2012, 8, 989–998.
- D. J. Peeters, G. G. Van den Eynden, P. J. van Dam, A. Prove, I. H. Benoy, P. A. van Dam, P. B. Vermeulen, P. Pauwels, M. Peeters, S. J. Van Laere and L. Y. Dirix, *Br. J. Cancer*, 2011, 104, 1472–1477.
- R. A. Harouaka, M. Nisic and S. Y. Zheng, *J. Lab. Autom.*, 2013, 18, 455–468.
- D. Marrinucci, K. Bethel, D. Lazar, J. Fisher, E. Huynh, P. Clark, R. Bruce, J. Nieva and P. Kuhn, *J. Oncol.*, 2010, 2010, 861341.
- M. Yu, A. Bardia, B. Wittner, S. L. Stott, M. E. Smas, D. T. Ting, S. J. Isakoff, J. C. Ciciliano, M. N. Wells, A. M. Shah, K. F. Concannon, M. C. Donaldson, L. V. Sequist, E. Brachtel, D. Sgroi, J. Baselga, S. Ramaswamy, M. Toner, D. A. Haber and S. Maheswaran, *Science*, 2013, 339, 580–584.
- S. L. Stott, C.-H. Hsu, D. I. Tsukrov, M. Yu, D. T. Miyamoto, B. A. Waltman, S. M. Rothenberg, A. M. Shah, M. E. Smas, G. K. Korir, F. P. Floyd, A. J. Gilman, J. B. Lord, D. Winokur, S. Springer, D. Irimia, S. Nagrath, L. V. Sequist, R. J. Lee, K. J. Isselbacher, S. Maheswaran, D. A. Haber and M. Toner, *Proc. Natl. Acad. Sci. U. S. A.*, 2010, 107, 18392–18397.
- C. Alix-Panabieres and K. Pantel, *Clin. Chem.*, 2013, 59, 110–118.
- A. Munaz, M. J. A. Shiddiky and N. T. Nguyen, *Biomicrofluidics*, 2018, 12, 031501.
- M. Hejazian, W. Li and N. T. Nguyen, *Lab Chip*, 2015, 15, 959–970.
- W. Zhao, R. Cheng, J. R. Miller and L. Mao, *Adv. Funct. Mater.*, 2016, 26, 3916–3932.
- M. A. Gijss, F. Lacharme and U. Lehmann, *Chem. Rev.*, 2010, 110, 1518–1563.
- N. Nguyen, *Nanofluidics*, 2012, 12, 1–16.
- N. Pamme, *Lab Chip*, 2006, 6, 24–38.
- Y. L. Zhou, D. T. Kumar, X. Y. Lu, A. Kale, J. DuBose, Y. X. Song, J. S. Wang, D. Q. Li and X. C. Xuan, *Biomicrofluidics*, 2015, 9, 044102.
- T. T. Zhu, R. Cheng, Y. F. Liu, J. He and L. D. Mao, *Microfluid. Nanofluid.*, 2014, 17, 973–982.
- W. J. Zhao, R. Cheng, S. H. Lim, J. R. Miller, W. Z. Zhang, W. Tang, J. Xie and L. D. Mao, *Lab Chip*, 2017, 17, 2243–2255.
- W. J. Zhao, R. Cheng, B. D. Jenkins, T. T. Zhu, N. E. Okonkwo, C. E. Jones, M. B. Davis, S. K. Kavuri, Z. L. Hao, C. Schroeder and L. D. Mao, *Lab Chip*, 2017, 17, 3097–3111.
- R. E. Rosensweig, *Ferrohydrodynamics*, Cambridge University Press, Cambridge, 1985.
- D. Wirtz, K. Konstantopoulos and P. C. Searson, *Nat. Rev. Cancer*, 2011, 11, 512–522.
- F. Fachin, P. Spuhler, J. M. Martel-Foley, J. F. Edd, T. A. Barber, J. Walsh, M. Karabacak, V. Pai, M. Yu, K. Smith, H. Hwang, J. Yang, S. Shah, R. Yarmush, L. V. Sequist, S. L. Stott, S. Maheswaran, D. A. Haber, R. Kapur and M. Toner, *Sci. Rep.*, 2017, 7, 10936.
- E. Ozkumur, A. M. Shah, J. C. Ciciliano, B. L. Emmink, D. T. Miyamoto, E. Brachtel, M. Yu, P. I. Chen, B. Morgan, J.

- Trautwein, A. Kimura, S. Sengupta, S. L. Stott, N. M. Karabacak, T. A. Barber, J. R. Walsh, K. Smith, P. S. Spuhler, J. P. Sullivan, R. J. Lee, D. T. Ting, X. Luo, A. T. Shaw, A. Bardia, L. V. Sequist, D. N. Louis, S. Maheswaran, R. Kapur, D. A. Haber and M. Toner, *Sci. Transl. Med.*, 2013, 5, 179ra147.
- 36 M. Yu, A. Bardia, N. Aceto, F. Bersani, M. W. Madden, M. C. Donaldson, R. Desai, H. L. Zhu, V. Comaills, Z. L. Zheng, B. S. Wittner, P. Stojanov, E. Brachtel, D. Sgroi, R. Kapur, T. Shioda, D. T. Ting, S. Ramaswamy, G. Getz, A. J. Iafrate, C. Benes, M. Toner, S. Maheswaran and D. A. Haber, *Science*, 2014, 345, 216–220.
- 37 B. L. Khoo, G. Greci, Y. B. Lim, S. C. Lee, J. Han and C. T. Lim, *Nat. Protoc.*, 2018, 13, 34–58.
- 38 D. Gao, I. Vela, A. Sboner, P. J. Iaquina, W. R. Karthaus, A. Gopalan, C. Dowling, J. N. Wanjala, E. A. Undvall, V. K. Arora, J. Wongvipat, M. Kossai, S. Ramazanoglu, L. P. Barboza, W. Di, Z. Cao, Q. F. Zhang, I. Sirota, L. Ran, T. Y. MacDonald, H. Beltran, J. M. Mosquera, K. A. Touijer, P. T. Scardino, V. P. Laudone, K. R. Curtis, D. E. Rathkopf, M. J. Morris, D. C. Danila, S. F. Slovin, S. B. Solomon, J. A. Eastham, P. Chi, B. Carver, M. A. Rubin, H. I. Scher, H. Clevers, C. L. Sawyers and Y. Chen, *Cell*, 2014, 159, 176–187.
- 39 N. M. Karabacak, P. S. Spuhler, F. Fachin, E. J. Lim, V. Pai, E. Ozkumur, J. M. Martel, N. Kojic, K. Smith, P. I. Chen, J. Yang, H. Hwang, B. Morgan, J. Trautwein, T. A. Barber, S. L. Stott, S. Maheswaran, R. Kapur, D. A. Haber and M. Toner, *Nat. Protoc.*, 2014, 9, 694–710.